Short-wavelength axion dark modes of cavity axion polariton

Yang Xiao [1], Huaiqiang Wang,[2] Dinghui Wang,[2] Xiaohong Yan,[3] and Haijun Zhang[2,4,*]

[1]*Department of Physics, Nanjing University of Aeronautics and Astronautics, Nanjing 210016, China*
[2]*National Laboratory of Solid State Microstructures and Physics School, Nanjing University, Nanjing 210093, China*
[3]*School of Material Science and Engineering, Jiangsu University, Zhenjiang 212013, China*
[4]*Collaborative Innovation Center of Advanced Microstructures, Nanjing University, Nanjing 210093, China*

The cavity axion polariton represents a new frontier in the field of topological matter and light-matter interactions. To realize strong axion-photon coupling and low damping of the axion mode, which are two key factors for quantum information applications, we studied the short-wavelength axion modes and the axion-axion interaction theoretically. Our results reveal an unconventional coupling between photon and standing wave axion modes that is in the strong-coupling regime as the number of antinodes is large. When two axion modes are coupled with cavity photons, cavity-mediated axion-axion coupling gives rise to the axion dark mode. Our results suggest that short-wavelength axion dark modes may be potential candidates for quantum manipulation and storage.

I. INTRODUCTION

Recently, many exotic phenomena of magnetic topological insulators have been revealed [1–5], especially the axion insulator state [2,6–9] and axion electrodynamics [10–22], which made a deep link between topological electronic states, magnetism, and optics. The axion quasiparticle emerges through the axion action $\mathcal{S}_{\text{topo}} = (\theta/2\pi)(e^2/hc_0) \int d^3x dt \mathbf{E} \cdot \mathbf{B}$ from the topological field theory [1,2], in which $\mathbf{E}$ and $\mathbf{B}$ are the electric field and magnetic induction inside the insulators, e is the charge of an electron, h is Planck's constant, c_0 is the speed of light in a vacuum, and θ (modulo 2π) is the dimensionless pseudoscalar parameter as the axion field. In antiferromagnetic topological insulators with breaking of both the time-reversal symmetry and the inversion symmetry, e.g., a van der Waals layer $Mn_2Bi_2Te_5$, $MnBi_2Te_4/Bi_2Te_3$ superlattices, and $MnBi_2Te_4$ films, most of which have been predicted and recently synthesized [9,23–30], the spin wave excitation generates a dynamical axion field $\theta(\boldsymbol{r}, t)$ [10,31]. Therefore, based on these materials, one can tune the properties of the antiferromagnetic spin wave to achieve the desired behavior of the dynamic axion field.

In the field of dynamical magnetism, a spin wave can be excited thermally or optically. At finite temperature and at equilibrium, thermally excited spin waves have a population that obeys the Bose-Einstein statistics. Temperature is the main factor of this mechanism. In contrast to a thermal spin wave, a spin wave excited by light or microwaves can be manipulated by photon frequency, polarization, power, etc. Hence optically excited spin waves present more tunability than thermal spin waves. An antiferromagnetic spin wave can be excited by terahertz-frequency photons, e.g., antiferromagnetic resonance [32,33], or by visible light, e.g., the

magnon Raman effect [34,35]. Here, magnons are the quanta of spin waves. The spin waves or magnons are in general related to transverse magnetization oscillations [36,37]. Axion quasiparticles in antiferromagnetic topological insulators have been predicted to originate from longitudinal magnetization oscillation [10,31]. More specifically, for magnetizations aligned along the z direction, the x and y components and the z component of magnetizations induce the spin wave (magnon) and dynamic axion field (axion), respectively. By shining a light with magnetic component parallel to the magnetization, one thus can achieve the longitudinal magnetization oscillation and dynamic axion field. Furthermore, when the light is confined inside a cavity, a cavity axion polariton is formed which reproduces a large axion-photon coupling [21]. These novel characteristics enable the cavity axion polariton to be used in axion-based quantum information manipulation and storage.

For the quantum control of light-matter interaction, the qubit in superconducting circuits [38] and the mechanical oscillator in cavity optomechanics [39] have been widely studied. In comparison to these two systems, the axion presents some advantages. First, the axion is described by the theories of topological matter and light-matter interaction. Based on the topological magnetoelectric effect [10], the axion-photon coupling is greatly enhanced near the topological phase transition. To achieve strong coupling, one can engineer the atomic structures of topological axion insulators and their superlattices to realize the transition from a topological trivial phase to a nontrivial phase [24]. Second, the axion frequency is in the terahertz frequency range, while the superconducting qubit and mechanical oscillator are in the gigahertz or megahertz frequency. Due to its higher frequency and smaller population, the axion is easier to cool to the ground state than the qubit and mechanical oscillator. Ground-state cooling is important to realize many quantum phenomena, e.g., quantum squeezing and entanglement [38,39]. Third, by introducing static

*zhanghj@nju.edu.cn
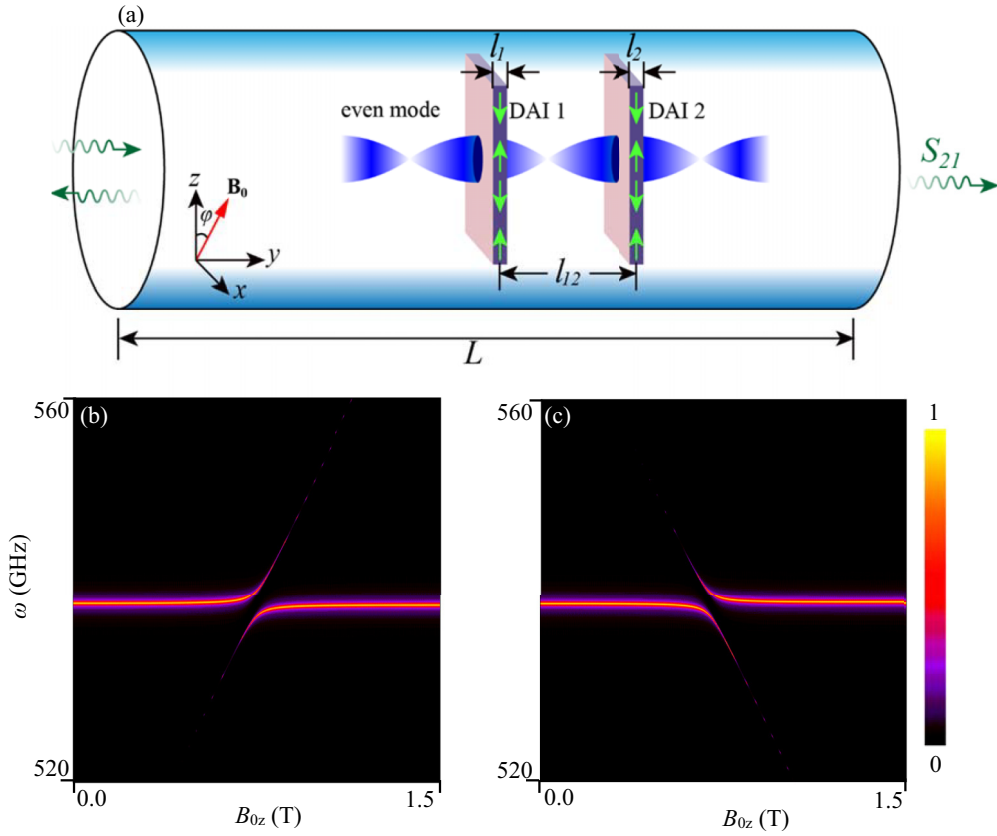
FIG. 1. (a) Schematic of the cavity geometry with two dynamical axion insulator (DAI) films. The photon propagates from the input port (left) to the output port (right) through two DAI films. We consider the even mode of cavity resonances in which the electric fields at the DAIs are the largest. A static magnetic field is applied with an angle φ with respect to the z axis and induces a coupling between the electric field **E** of the photon and the dynamical axion field $\delta\theta$. l_1, l_2, and l_{12} are the thickness of DAI1, the thickness of DAI2, and the distance between them. L is the length of the cavity. The light green arrows show the antiferromagnetic sublattice magnetizations. (b) and (c) $|S_{21}|$ transmission spectra of long-wavelength β_+ (b) and β_- (c) axion modes. The zero-field axion frequency is 498.6 GHz in (b) and 576 GHz in (c).

magnetic field **B**$_0$ and setting **B** = **B**$_0$ in $\mathcal{S}_{\text{topo}}$, one can see that the axion-photon coupling strength is proportional to B_0. This provides an easy way of tuning axion-photon coupling by varying the static magnetic field.

For quantum information applications, strong coupling and low damping are two key factors [40]. Strong coupling between axion and photon modes has been predicted for the long-wavelength axion mode [21]. In general, there exists only one long-wavelength axion mode with almost zero wave vector. The short-wavelength axion mode has a finite wave vector, which provides a number of possibilities for axion mode selection. However, it is still unclear whether strong coupling can be realized for short-wavelength axion modes. On the other hand, in order to obtain low damping, the dark mode is usually employed. In quantum optics [40], the interference can result in a dark mode for which two modes destructively interfere. Due to extremely weak coupling with the surrounding environment, the dark mode can be used for the storage of information, which has been extensively studied in atomic, magnonic, superconducting qubit, and optomechanical systems [41–43]. Therefore it is physically meaningful to study the short-wavelength axion modes and the axion dark modes of cavity axion polaritons.

The remainder of this paper is organized as follows. In Sec. II, we provide a comprehensive description of theoretical and methodological details of coupling between cavity photon and short-wavelength axion modes. Section III is devoted to the presentation and interpretation of our numerical results for the short-wavelength cavity axion polariton. Conclusions are drawn from the findings in Sec. IV.

II. THEORY AND METHOD

A. Short-wavelength axion modes

The dynamical equations of a short-wavelength axion polariton are written as [10]

$$\frac{\partial^2 \mathbf{E}}{\partial t^2} - c^2 \nabla^2 \mathbf{E} + \frac{\alpha}{\pi \epsilon} \frac{\partial^2 \delta\theta}{\partial t^2} \mathbf{B}_0 = 0, \quad (1)$$

$$\frac{\partial^2 \delta\theta}{\partial t^2} - v^2 \nabla^2 \delta\theta + m^2 \delta\theta + \Gamma \frac{\partial \delta\theta}{\partial t} - \frac{\alpha}{8\pi^2 g^2 J} \mathbf{B}_0 \cdot \mathbf{E} = 0, \quad (2)$$

where **B**$_0$ is the static magnetic field inside the insulators. ϵ is the dielectric constant, $c = c_0/\sqrt{\epsilon\mu}$ is the speed of light in the dynamical axion insulator (DAI), and μ is the magnetic permeability. $\alpha = e^2/\hbar c_0$ is the fine-structure constant.

The axion field $\theta = \theta_0 + \delta\theta$, in which θ_0 and $\delta\theta$ are the static and dynamic parts of the axion field. The dynamic part originates from the longitudinal magnetization excitation with material-dependent stiffness J, velocity v, mass (frequency) m, and coefficient g [10]. Γ is the intrinsic damping of axion modes. In the above equations, the magnetic component of the electromagnetic field is much smaller than the static field $\mathbf{B}_0$ and thus is neglected.

As predicted in Ref. [10], the dynamic axion field $\delta\theta$ is expressed by

$$\delta\theta \propto (M_z^A - M_z^B), \tag{3}$$

where M_z^A and M_z^B are the z components of sublattice magnetizations $\mathbf{M}^A$ and $\mathbf{M}^B$ of an antiferromagnet. The saturation magnetizations of two sublattices are along the z direction. Equation (3) indicates that the dynamic axion field is physically equivalent to the longitudinal magnetization oscillations. In the field of magnetization dynamics, such longitudinal oscillation can be achieved by parallel pumping, in which the oscillating field is parallel to the magnetizations [21]. Based on the antiferromagnetic parallel pumping theory [44], the frequency of longitudinal magnetization oscillation is $\omega^\parallel = 2\omega_0 \pm 2\gamma B_{0z}$, where γ is the gyromagnetic ratio and B_{0z} is the z component of $\mathbf{B}_0$. ω_0 is the zero-field frequency of antiferromagnetic resonance and is determined by the exchange field and anisotropic field in an antiferromagnet [36]. So, we have $m = \omega^\parallel$. For the sake of convenience, we refer to the mode with $m = m_0 + 2\gamma B_{0z}$ and the mode with $m = m_0 - 2\gamma B_{0z}$

as β_+ and β_- axion modes, respectively. Here, we define $m_0 = 2\omega_0$. Moreover, Eq. (3) is derived based on antiferromagnetic collinear magnetism. At a high magnetic field, the spin-flop transition occurs, and sublattice magnetizations become canted [45], which may invalidate Eq. (3). Therefore the magnetic field used in this paper is not so high that spin-flop transition will not occur.

The last terms of Eqs. (1) and (2) represent the axion-photon coupling. To have nonvanishing coupling, the term of $\mathbf{B}_0 \cdot \mathbf{E}$ cannot be zero. Since the dynamic magnetic field resulting in longitudinal magnetization oscillation is along the z axis, the dynamic electric field $\mathbf{E}$ is assumed to be in the x axis. This indicates that the static magnetic field $\mathbf{B}_0$ has an x component B_{0x}. On the other hand, B_{0z} is necessary for the axion frequency. Therefore the static magnetic field is oriented with an angle φ with respect to the z axis in the x-z plane. The electromagnetic waves propagate along the y axis. With these considerations, Eqs. (1) and (2) can be converted into a scalar form

$$\frac{\partial^2 E}{\partial t^2} - c^2 \nabla^2 E + \frac{\alpha B_{0x}}{\pi\epsilon} \frac{\partial^2 \delta\theta}{\partial t^2} = 0, \tag{4}$$

$$\frac{\partial^2 \delta\theta}{\partial t^2} - v^2 \nabla^2 \delta\theta + m^2 \delta\theta + \Gamma \frac{\partial \delta\theta}{\partial t} - \frac{\alpha B_{0x}}{8\pi^2 g^2 J} E = 0. \tag{5}$$

By considering the position and time dependence of E and $\delta\theta$, i.e., $e^{-i\omega t + iky}$, we solve Eqs. (4) and (5) simultaneously and obtain two propagation states

$$c^2 k_\pm^2 = \frac{[v^2\omega^2 + (\omega^2 + i\Gamma\omega - m^2)] \pm \sqrt{[v^2\omega^2 - (\omega^2 + i\Gamma\omega - m^2)]^2 + 4b^2\omega^2 v^2}}{2v^2}, \tag{6}$$

where $b = \sqrt{\alpha^2 B_{0x}^2 / 8\pi^3 \epsilon g^2 J}$ and $\nu = \frac{v}{c}$. One can calculate the ω-k relation and achieve an anticrossing gap, which is a key feature of the polariton system. The size of anticrossing gap is related to the parameter b which reflects the coupling strength of the axion-photon coupling. The theory and method of determining the value of b for $MnBi_2Te_4$-based DAIs are given in our previous paper [21]. When $\nu = 0$, i.e., $v = 0$, the propagation state of k_- corresponds to the long-wavelength axion mode. Another state with $k_+ \to \infty$ becomes unphysical and thus is omitted.

B. Transfer matrix

Our next task is to deal with the propagation of an electromagnetic wave in a DAI-embedded cylindrical cavity, which is shown in Fig. 1(a). To do so, we need to calculate the transfer matrix with the propagation states given in Eq. (6). We first discuss the transfer matrix of the long-wavelength axion mode since it has only one propagation state in the DAI. With the state k_-, the electric and magnetic fields are written as

$$B = (B^+ e^{-iky} + B^- e^{iky}), \tag{7}$$

$$E = Z(B^+ e^{-iky} - B^- e^{iky}), \tag{8}$$

where $Z = \frac{E}{B} = -\frac{\omega}{k}$ is the impedance, $k = k_-$ as $\nu = 0$, and B^+ and B^- are the amplitudes of right-going and left-going waves, respectively.

The magnetic and electric fields at the left ($y = 0$) and right ($y = l_s$) surfaces of a DAI layer are

$$B_{y=0} = (B^+ + B^-)$$
$$E_{y=0} = Z(B^+ - B^-)$$
$$B_{y=l_s} = (B^+ e^{-ikl_s} + B^- e^{ikl_s})$$
$$E_{y=l_s} = Z(B^+ e^{-ikl_s} - B^- e^{ikl_s}). \tag{9}$$

The transfer matrix connecting the fields at $y = 0$ and $y = l_s$ is defined as

$$\begin{pmatrix} E_{y=l_s} \\ B_{y=l_s} \end{pmatrix} = T_s \begin{pmatrix} E_{y=0} \\ B_{y=0} \end{pmatrix}. \tag{10}$$

From Eq. (9), one can obtain the transfer matrix

$$T_s = \begin{pmatrix} \cos(kl_s) & -jZ\sin(kl_s) \\ -\frac{j}{Z}\sin(kl_s) & \cos(kl_s) \end{pmatrix}. \tag{11}$$

Once the transfer matrix is obtained, the propagation of an electromagnetic wave in a cavity or waveguide can be easily treated. The derivations of the transfer matrix for

long-wavelength axion modes were presented in our previous work [21].

As for short-wavelength axion modes, we have $\nu \neq 0$. There are two propagation states with $k_\pm$ inside the DAI according to Eq. (6). The electric and magnetic fields are written as a linear combination of these two propagation states, i.e.,

$$B = \sum_{n=1}^{2} (B_n^+ e^{-ik_n y} + B_n^- e^{ik_n y}),$$

$$E = \sum_{n=1}^{2} Z_n (B_n^+ e^{-ik_n y} - B_n^- e^{ik_n y}),$$

where $n = 1$ and $n = 2$ refer to k_+ and k_-.

The fields at the left ($y = 0$) and right ($y = l_s$) surfaces of the DAI are

$$B_{y=0} = \sum_{n=1}^{2} (B_n^+ + B_n^-)$$

$$E_{y=0} = \sum_{n=1}^{2} Z_n (B_n^+ - B_n^-)$$

$$B_{y=l_s} = \sum_{n=1}^{2} (B_n^+ e^{-ik_n l_s} + B_n^- e^{ik_n l_s})$$

$$E_{y=l_s} = \sum_{n=1}^{2} Z_n (B_n^+ e^{-ik_n l_s} - B_n^- e^{ik_n l_s}). \tag{12}$$

.

Obviously, the above four equations, i.e., Eqs. (12), are insufficient to derive the transfer matrix, and thus two extra equations are required. This is accomplished by introducing the boundary conditions of the axion field at the surfaces. The simplest boundary condition of the axion field is written as [46–48]

$$\delta\theta_{y=0} = 0, \tag{13}$$

$$\delta\theta_{y=l_s} = 0, \tag{14}$$

indicating that the axion fields at surfaces are totally vanishing.

With Eq. (4), the relation between E and $\delta\theta$ is given by

$$\delta\theta = Q \cdot E, \tag{15}$$

where $Q = \frac{\epsilon\pi(c^2k^2-\omega^2)}{\alpha B_{0x}\omega^2}$.

The boundary conditions in Eqs. (13) and (14) are rewritten as

$$\sum_{n=1}^{2} Z_n Q_n (B_n^+ - B_n^-) = 0$$

$$\sum_{n=1}^{2} Z_n Q_n (B_n^+ e^{-ik_n l_s} - B_n^- e^{ik_n l_s}) = 0. \tag{16}$$

To obtain the transfer matrix, we combine Eq. (16) and the third and the fourth equations of Eq. (12) to construct a matrix equation

$$(J) \begin{pmatrix} B_1^+ \\ B_1^- \\ B_2^+ \\ B_2^- \end{pmatrix} = \begin{pmatrix} B_{y=l_s} \\ E_{y=l_s} \\ 0 \\ 0 \end{pmatrix}, \tag{17}$$

where J is written as

$$J = \begin{pmatrix} e^{-ik_1 l_s} & e^{ik_1 l_s} & e^{-ik_2 l_s} & e^{ik_2 l_s} \\ Z_1 e^{-ik_1 l_s} & -Z_1 e^{ik_1 l_s} & Z_2 e^{-ik_2 l_s} & -Z_2 e^{ik_2 l_s} \\ Z_1 Q_1 & -Z_1 Q_1 & Z_2 Q_2 & -Z_2 Q_2 \\ Z_1 Q_1 e^{-ik_1 l_s} & -Z_1 Q_1 e^{ik_1 l_s} & Z_2 Q_2 e^{-ik_2 l_s} & -Z_2 Q_2 e^{ik_2 l_s} \end{pmatrix}. \tag{18}$$

With Eq. (17), we can express $B_{1,2}^\pm$ with $B_{y=l_s}$ and $E_{y=l_s}$ and then substitute them into the first and the second equations of Eq. (12). Therefore the transfer matrix is given by

$$T_s = \begin{pmatrix} A & B \\ C & D \end{pmatrix}^{-1}, \tag{19}$$

where

$$A = Z_1 I_{12} - Z_1 I_{22} + Z_2 I_{32} - Z_2 I_{42},$$

$$B = Z_1 I_{11} - Z_1 I_{21} + Z_2 I_{31} - Z_2 I_{41},$$

$$C = I_{12} + I_{22} + I_{32} + I_{42},$$

$$D = I_{11} + I_{21} + I_{31} + I_{41}.$$

Here, the matrix I is the inverse of matrix J. I_{nm} is the element in the nth row and the mth column of matrix I.

C. Transmission coefficient

In Fig. 1(a), the cavity is driven by external sources through the input port, and the signal emitted from the output port is further analyzed by other external circuits and components. The ratio of amplitudes of transmitted and incident waves is defined as transmission coefficient S_{21}. To induce cavity resonance, i.e., a standing wave, we consider strong reflection at the input and output ports with reflectivity $R \approx 1$. Depending on the number of antinodes of the standing wave, the cavity resonance can be either even mode and odd mode. In this paper, only even mode is considered since it has strong axion-photon coupling. Inside the cavity, two DAIs, i.e., DAI1 and DAI2, are placed at two antinodes of even mode. The DAI layers are perpendicular to the propagation direction of the electromagnetic wave in order to achieve strong axion-photon coupling. The thicknesses of the DAIs are l_1 and l_2, and the distance between the two DAIs is l_{12}. In this paper, we consider small thicknesses of DAI layers compared with the

cavity length L, i.e., $l_{1,2} \ll L$, so that the sinusoidal functions in Eq. (11) and the exponential functions in Eq. (18) can be approximated to the linear order. In such a case, the axion and photon modes are linearly coupled, and the coupling strength is linearly proportional to $\sqrt{l_{1,2}}$. As the thickness increases further, the high-order terms of sinusoidal and exponential functions will play roles, reproducing the nonlinear effect [21].

The magnetic and electric fields at the input and output ports are connected by a full transfer matrix which is written as $T = T_{0a}T_{s1}T_{0b}T_{s2}T_{0c}$. T_{s1} and T_{s2} are transfer matrices of DAI1 and DAI2 and are calculated from Eq. (19). $T_{0a,0b,0c}$ is the transfer matrix in the air region between the input port and DAI1 (0a), between DAI1 and DAI2 (0b), and between DAI2 and the output port (0c). The transfer matrix of the air region is obtained by replacing in Eq. (11) the quantities k, Z, and $l_{1,2}$ with those of the air region, i.e., $k_0 = \frac{\omega}{c_0}$, $Z_0 = -c_0$, and l_0. l_0 is the length of the air regions. With the transfer matrix T, we can build the scattering matrix which gives the relation between the amplitudes of the incident wave at the input port and those of the transmitted wave at the output port and then calculate the transmission coefficient S_{21}.

D. Parameters

In the numerical calculations, we set the values of parameters as follows. We take the dielectric constant $\epsilon = 15$, the permeability $\mu = 1$, the length of the cavity $L = 5$ mm, the thickness $l_1 = l_2 = 1$ μm for the two DAIs, the distance between the two layers $l_{12} = 0.277$ mm, the reflectivity at the two ports $R = 0.99$, and the intrinsic damping of the axion $\Gamma = 2.4$ GHz. The frequency of the cavity resonance is 538.5 GHz. The velocity of the axion is $v = 5 \times 10^{-4}c$. The coupling strength $b = 48.5$ GHz at $B_{0x} = 1$ T. The axion frequency at zero magnetic field varies for different systems and is given in each figure. The values of parameters are the same as those used in Ref. [21].

III. RESULTS AND DISCUSSION

A. Single DAI layer

We first briefly discuss the results of long-wavelength axion modes which have been studied in our previous work [21]. As shown in Figs. 1(b) and 1(c), we consider the β_+ ($m_{\beta_+} = m_{0\beta_+} + 2\gamma B_{0z}$) and β_- ($m_{\beta_-} = m_{0\beta_-} - 2\gamma B_{0z}$) axion modes. The frequencies of axion modes increase or decrease with the static magnetic field and cross the cavity resonance with an anticrossing gap. The well-resolved anticrossing gap indicates that the axion-photon system is in the strong-coupling regime. The size of the anticrossing gap is determined by the parameter b.

Next we show the results of the short-wavelength axion mode and axion dark modes, which are the main results of this work. Figure 2 shows the $|S_{21}|$ spectra of standing wave β_+ and β_- axion modes for a single DAI layer. The spectrum displays many axion modes. Due to nonuniform axion distribution, the axion field is written as $\delta\theta = A_1 \cos(ky) + A_2 \sin(ky)$ with two coefficients $A_{1,2}$. The boundary conditions in Eqs. (13) and (14) imply $A_1 = 0$ and $k = n\frac{\pi}{l_s}$ with integer n. So, the axion modes are standing wave modes with

finite wavelength. Moreover, only the standing wave modes with odd integer n couple with the photon. As n is even, the function $\delta\theta \propto \sin(n\frac{\pi}{l_s}y)$ has $\frac{n}{2}$ positive regions [blue color in Fig. 2(c)] and $\frac{n}{2}$ negative regions [light pink color in Fig. 2(c)]. When coupling with the photon mode, the positive and negative regions cancel each other. However, for odd integer n, there are $\frac{n+1}{2}$ positive regions and $\frac{n-1}{2}$ negative regions. There is always one positive region which participates in the axion-photon coupling. The above analysis indicates that the discrete modes in Figs. 2(a) and 2(b) are the odd-order standing wave axion modes.

Based on Eq. (5), one can see that the resonance frequency of the standing wave axion mode is given by $m^2 = (m_0 \pm 2\gamma B_{0z})^2 + (n^2\frac{\pi^2 v^2}{l_s^2})^2$ for β_+ and β_- modes. At a given frequency m, as B_{0z} increases, the mode integer n decreases for the β_+ mode while it increases for the β_- mode. On the other hand, the coupling strength b is proportional to the static magnetic field B_0. As n increases, the magnetic field B_{0z}, the coupling strength, and the size of the anticrossing gap for the β_+ mode decrease as shown in Fig. 2(a). However, for the β_- mode, one can see that the size of the anticrossing gap remains almost constant except for the $n = 1$ mode. The reasons are twofold and are depicted in Fig. 2(c). The first is the increase in B_{0z} and coupling strength as n increases. The second is the fact that the part of the axion field participating in the axion-photon interaction decreases according to the scaling of $\propto \frac{1}{n}$. The behavior of the β_+ mode is analogous to those found in magnon-photon coupled systems [47–49]. Due to the small coupling strength, the high-n standing wave β_+ modes are not suitable for axion polariton applications. However, the β_- mode presents an unconventional feature of the coupling between photon and high-n standing wave modes, providing a possibility of using the high-n standing wave for future applications of axion detection and manipulation.

B. Two DAI layers

The above discussion is for a single DAI layer with only one axion mode. We next present the results when there are two DAI layers inside the cavity and discuss the axion-axion interference effect. In Fig. 3(a), two β_+ axion modes have the same frequency, i.e., $m_1 = m_2$. One can see that the spectrum displays only two modes even though three modes (one cavity mode and two axion modes) are involved in the interaction. However, in Fig. 3(b), where the two axion modes have distinct frequencies, three modes appear in the spectrum. In order to understand this behavior, we consider the dynamical part of the axion action of $S \propto \delta\theta \mathbf{E} \cdot \mathbf{B}_0$ and quantize the dynamical axion field $\delta\theta$ and dynamic electric field $\mathbf{E}$ as the axion and photon based on the standard second-quantization procedure. The Hamiltonian takes the form of

$$H = \omega_a a^\dagger a + \omega_c c^\dagger c + g(a^\dagger c + c^\dagger a), \quad (20)$$

where a ($a^\dagger$) and c ($c^\dagger$) are annihilation (creation) operators of axion and photon modes with resonance frequency of ω_a and ω_c. g is the coupling strength of the axion-photon interaction. In the presence of two axion modes, the Hamiltonian is
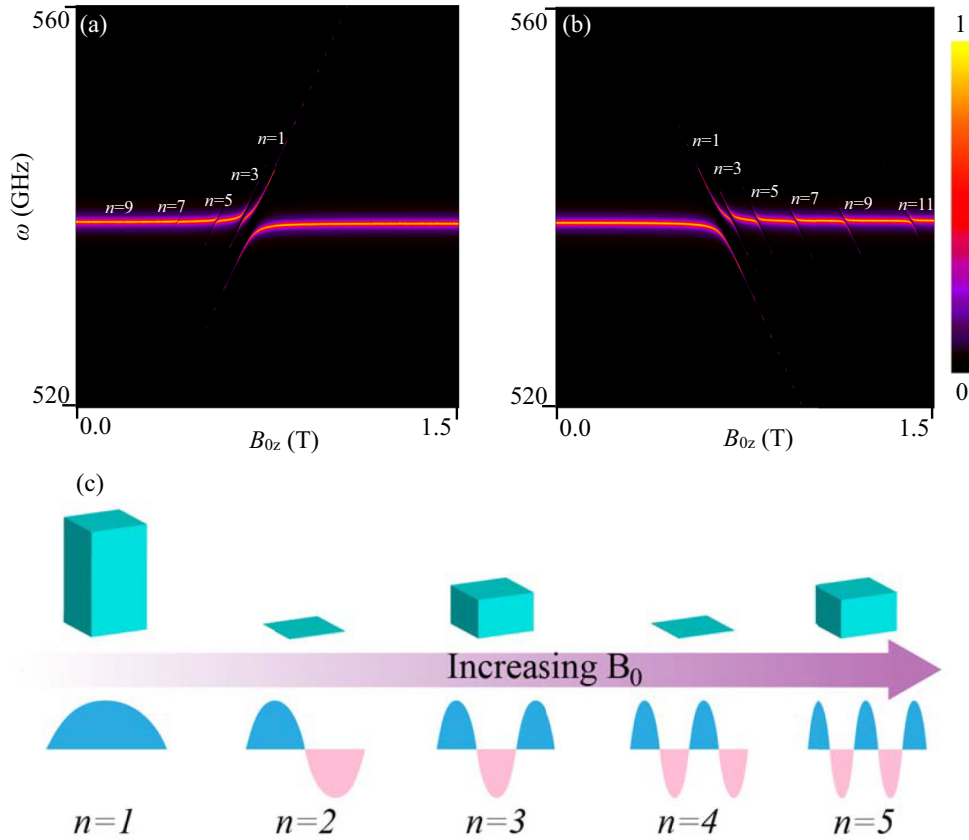
FIG. 2. $|S_{21}|$ transmission spectra of short-wavelength (a) β_+ and (b) β_- axion modes for which the axion frequencies increase or decrease with magnetic field. The zero-field axion frequency is 498.6 GHz in (a) and 576 GHz in (b). (c) As the number of antinodes n increases, even-n modes do not couple with the cavity photons because the positive (blue color) and negative (light pink color) regions of the axion field cancel each other. For the odd-n mode, only $\frac{1}{n}$ of dynamical axion field participates in the axion-photon coupling, and thus the coupling strength decreases with increasing n. On the other hand, the coupling strength is proportional to the magnetic field and thus increases with n for the β_- axion mode. The above two factors result in the behavior that the anticrossing gaps of large-n axion modes remain almost unchanged in (b).

rewritten as

$$
\begin{aligned}
H = {} & \omega_a a^\dagger a + \omega_b b^\dagger b + \omega_c c^\dagger c \\
& + g_a(a^\dagger c + c^\dagger a) + g_b(b^\dagger c + c^\dagger b),
\end{aligned}
\tag{21}
$$

where b $(b^\dagger)$, ω_b, and g_b are the annihilation (creation) operator, resonance frequency, and coupling strength of the second axion mode.

To obtain the eigenfrequencies, we write the equation of motion of Eq. (21)

$$
\frac{d}{dt}\begin{pmatrix} a \\ b \\ c \end{pmatrix} = -i \begin{pmatrix} \omega_a & 0 & g_a \\ 0 & \omega_b & g_b \\ g_a & g_b & \omega_c \end{pmatrix} \begin{pmatrix} a \\ b \\ c \end{pmatrix}.
\tag{22}
$$

By diagonalizing the matrix in Eq. (22), we obtain three eigenfrequencies as $\omega_a = \omega_b$

$$
\omega_1 = \omega_a,
\tag{23}
$$

$$
\omega_{2,3} = \frac{\omega_a + \omega_c \pm \sqrt{(\omega_a - \omega_c)^2 + 4G^2}}{2},
\tag{24}
$$

where $G = \sqrt{g_a^2 + g_b^2}$. In the transmission spectrum shown in Fig. 3(a), the modes with frequency $\omega_{2,3}$ appear, while the

mode of ω_1 does not occur. To understand this behavior, we consider an operator transformation

$$
B = \frac{g_a a + g_b b}{G},
\tag{25}
$$

$$
D = \frac{g_b a - g_a b}{G}
\tag{26}
$$

for the bright (B) and dark (D) modes. As $\omega_a = \omega_b$, the Hamiltonian Eq. (21) is transformed into $H = \omega_a B^\dagger B + \omega_a D^\dagger D + \omega_c c^\dagger c + G(cB^\dagger + Bc^\dagger)$. The dark mode D does not couple with the photon mode c, and thus it does not appear in the photon transmission spectrum. The axion dark mode represents a complete destructive interference of two axion modes which is mediated by the photon mode. The condition of $\omega_a = \omega_b$ is similar to those used to generate the interference from two sources of optical waves, mechanical waves, and even microscopic particles [50]. If $\omega_a \neq \omega_b$ in Fig. 3(b), the interference condition is no longer met, and thus the dark mode occurs in the spectrum. Figures 3(c) and 3(d) show the transmission spectra of one β_+ axion mode and one β_- axion mode. In contrast to two β_+ axion modes, the β_+ and β_- modes have the same frequencies at the crossing point only. Therefore the axion dark mode occurs at this point.
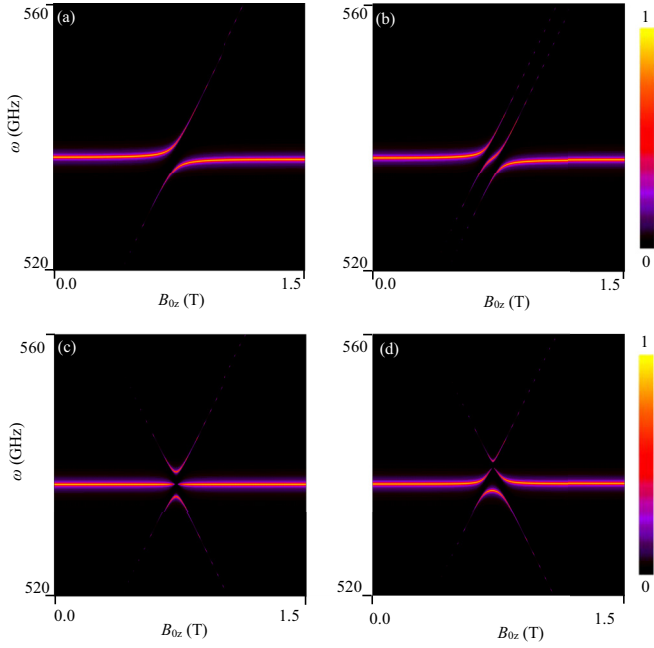
FIG. 3. $|S_{21}|$ transmission spectra of two long-wavelength axion modes. The zero-field frequencies of the two modes are 498.6 and 498.6 GHz in (a), 496.2 and 501 GHz in (b), 498.6 and 576 GHz in (c), and 501 and 578.5 GHz in (d).

FIG. 4. $|S_{21}|$ transmission spectra of (a) and (b) long-wavelength β_+ and short-wavelength β_- modes, (c) short-wavelength β_+ and β_- modes, and (d) two short-wavelength β_- modes. The zero-field axion frequencies are 498.6 and 576 GHz in (a), 489 and 576 GHz in (b), 498.6 and 576 GHz in (c), and 576 and 576.5 GHz in (d).

The above results can be used to enhance the axion-photon coupling and reduce the axion dissipation. In the field of quantum optics, strong coupling and a low damping rate are usually prerequisites of quantum manipulation and information storage [40]. On the one hand, one can extend our results to the case of N DAI layers in which the coupling between the bright axion mode and the photon is given by $G = \sqrt{\sum_i g_i^2}$. By increasing the number N, one can enhance the axion-photon coupling. On the other hand, the axion dark mode does not couple with the photon mode and thus is insensitive to the external electromagnetic perturbation. Therefore the axion dark mode can store the information for a long time.

Finally, we present the results of short-wavelength axion dark modes. Figure 4(a) shows the transmission spectrum of one long-wavelength β_+ mode and many short-wavelength β_- standing wave modes. Due to the positive and negative slopes of the mode curves, two kinds of modes cross at many different magnetic fields and frequencies. This is an advantage over the coupling of two long-wavelength β_+ and β_- modes, for which only one crossing point appears. In Fig. 4(a), one can see three types of couplings. The first is the axion-photon coupling as discussed in previous sections. The second is the cavity-mediated axion dark mode of the long-wavelength β_+ mode and $n = 1$ standing wave axion mode. The vanishing transmission due to destructive interference can be clearly seen at the crossing point of the two modes. The third coupling results in a small anticrossing gap between the long-wavelength β_+ mode and $n = 3, 5$ standing wave β_- mode. For $n = 7$ and above, the gap is negligible and cannot be appreciated. To understand this behavior, we rewrite
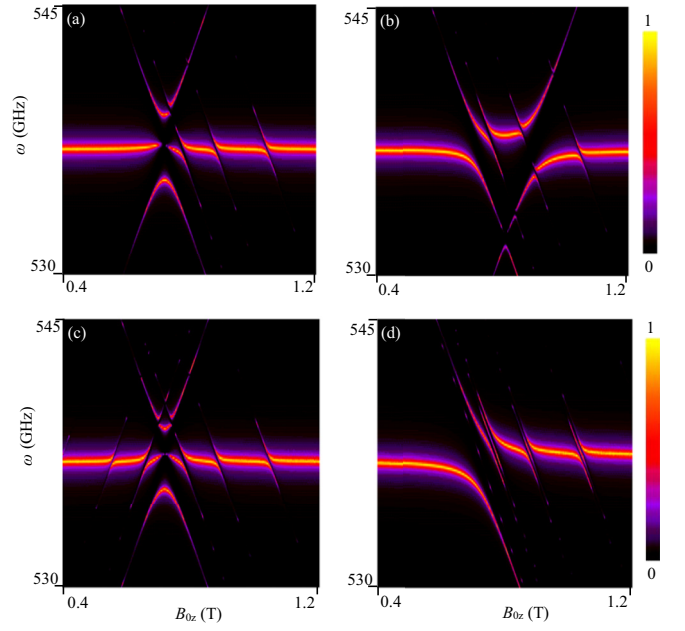
Eq. (22) as

$$\frac{da}{dt} = -i\omega_a a - ig_a c, \tag{27}$$

$$\frac{db}{dt} = -i\omega_b b - ig_b c, \tag{28}$$

$$\frac{dc}{dt} = -i\omega_c c - ig_a a - ig_b b. \tag{29}$$

For the third coupling, one can see from Fig. 4(a) that the detuning $\omega_c - \omega$ at the anticrossing point is large. In such a case, one can adiabatically eliminate the cavity mode, i.e., $\frac{dc}{dt} = 0$, and then obtain $c = -\frac{g_a}{\omega_c}a - \frac{g_b}{\omega_c}b$. Substituting c into Eqs. (27) and (28), we obtain

$$\frac{da}{dt} = -i\left(\omega_a - \frac{g_a^2}{\omega_c}\right)a + i\frac{g_a g_b}{\omega_c}b, \tag{30}$$

$$\frac{db}{dt} = -i\left(\omega_b - \frac{g_b^2}{\omega_c}\right)b + i\frac{g_a g_b}{\omega_c}a, \tag{31}$$

where the second terms on the right-hand side of Eqs. (30) and (31) imply an effective Hamiltonian

$$H_{\text{eff}} = \omega'_a a^\dagger a + \omega'_b b^\dagger b + g_{\text{eff}}(a^\dagger b + b^\dagger a), \tag{32}$$

where $\omega'_{a,b} = \omega_{a,b} - \frac{g_{a,b}^2}{\omega_c}$ and $g_{\text{eff}} = \frac{g_a g_b}{\omega_c}$. Equation (32) indicates that a dispersive coupling between axion modes and the cavity photon leads to an indirect axion-axion coupling. Due to $\omega_c \gg g_{a,b}$, the effective axion-axion coupling strength g_{eff} is small, which is in agreement with the small anticrossing gap in Fig. 4(a).

Moreover, one can alter the axion mode spectrum to tune the frequency and magnetic field at which the coupling occurs. As seen in Fig. 4(b), we shift down the frequency of two

axion modes and see that the couplings appear at various fields and frequencies. Figure 4(c) shows the coupling of the cavity photon and the short-wavelength β_+ and β_- axion modes. A prominent feature is that more anticrossing gaps and coupling appear than in the presence of long-wavelength axion modes. Also, we show the coupling between two short-wavelength β_- axion modes. Since the two modes have different frequencies, they do not give rise to the axion dark mode.

C. Discussion

In the field of magnon-photon [51–56] and magnon-magnon [57–59] interaction, the coupling between cavity photon and long-wavelength magnon modes has been extensively studied. The magnon dark mode has been demonstrated in a cavity with multiple magnon modes [43]. Moreover, direct magnon-magnon coupling has been observed in recent experiments with hybrid ferromagnetic nanostructures [57–59]. Among them, the long-wavelength magnon mode and short-wavelength standing wave magnon modes couple strongly due to the interlayer exchange and dipolar interaction. This is similar to our results in Figs. 4(a) and 4(b). The difference between this paper and Refs. [57–59] is that the coupling described in this paper is mediated by cavity photons. The results of two short-wavelength axion modes shown in Figs. 4(c) and 4(d) have not been observed or predicted in the field of magnons. Our results indicate that the cavity axion polariton with short wavelength is an excellent test bed for achieving different types of axion-photon couplings.

It is important to make a comparison between this paper and Ref. [21]. Although both works study cavity axion polaritons, they differ in several aspects. First, this paper focuses on the short-wavelength axion modes and axion-axion interference, while Ref. [21] studied a single long-wavelength axion mode. Second, these two works reveal different physics. This paper studies level repulsion due to linear axion-photon interaction, while Ref. [21] considered nonlinearity-induced level attraction. Third, the methods used in these two works are distinct. In Ref. [21], the long-wavelength axion mode has only one wave vector, which is calculated by combining the Maxwell's equations and axion dynamic equation. The analytic expression of the transfer matrix can be easily obtained with one wave vector. However, in this paper, the short-wavelength axion mode has two wave vectors. In order to obtain the transfer matrix, we have to introduce the axion boundary condition and make a numerical calculation.

We next discuss the effect of temperature and external electromagnetic field on the frequency and damping of the axion dark mode, which are important for axion-based quantum information applications. As mentioned in Sec. II A, the axion frequency m is related to the antiferromagnetic resonance frequency ω_0 which is determined by the exchange and anisotropic fields of an antiferromagnet [36]. As the temperature decreases, the anisotropic field increases [33], and thus the axion frequency m will increase. As for the axion damping, it presents more complicated behaviors than the axion frequency. First, the intrinsic damping usually decreases with the decreasing temperature and in some special cases increases with decreasing temperature at low temperature [52]. These distinct behaviors depend on the scattering with the

phonon, impurity, two-level systems, etc. [52]. Therefore the intrinsic damping of the axion dark mode depends on the dominant scattering process, which could be demonstrated in future experiments. Second, a traveling wave is an electromagnetic environment which can coexist with a standing wave (cavity resonance) in the cavity [60]. The decay of the axion into traveling waves can give rise to extra damping of the axion. Moreover, the simultaneous decays of axion and cavity photons into traveling waves may result in dissipative axion-photon coupling, which has been observed in a recent study of magnon-photon coupling [60]. Third, the coherence length $\mathcal{L}_c$ of cavity photons is crucial for quantum information transfer between axion modes on two DAI layers. $\mathcal{L}_c = \frac{\lambda}{2}Q_c$ with the wavelength of light λ and the quality factor of the cavity Q_c. For a cavity with resonance frequency of 300 GHz, we have $\lambda = 1$ mm and $Q_c \approx 10^3$ [61]. Thus the coherence length of $\mathcal{L}_c \approx 1$ m is much larger than the distance ($l_{12} = 0.277$ mm) between the two DAI layers, which indicates that the axion state can be transferred coherently between the two DAI layers.

Recent progress in terahertz-frequency photon sources and magnetic topological insulators make possible our proposal of a short-wavelength cavity axion polariton. A cavity with resonance frequency up to 4 THz [61] has been reported, which displays strong coupling and low dissipation. Moreover, many $MnBi_2Te_4$-based magnetic topological materials have been discovered and offer a promising platform for the study of axion electrodynamics [8,9,23–30,62–71]. The large dynamical axion field of these materials is key to realizing the proposal of a axion dark mode in this paper.

IV. CONCLUSIONS

In summary, we investigated the cavity axion polariton in the presence of short-wavelength axion modes and axion-axion interference. In contrast to long-wavelength axion modes studied in previous work, we find that the fully pinned boundary condition at the surfaces results in the occurrence of a series of standing wave axion modes. For one type of standing wave modes, the axion-photon coupling strength decreases rapidly as the number of antinodes increases. However, for another type of modes, the coupling strength remains almost unchanged, which makes possible the use of high-order standing wave axion modes in the detection of axion quasiparticles. Moreover, when two long-wavelength or two short-wavelength axion modes are coupled with cavity photons, one can achieve the axion dark mode under the condition that the two axion modes have equal frequencies. As one long-wavelength axion mode and one short-wavelength axion mode are present, one can obtain the direct axion-photon coupling, cavity-mediated axion dark mode, and axion-axion coupling. The latter two couplings can be tuned by frequency detuning and the magnetic field. Our results provide much insight into the study of the cavity axion polariton of short-wavelength axion modes and can find applications in the fields of axion-based quantum information manipulation and storage.

ACKNOWLEDGMENTS

[1] X.-L. Qi and S.-C. Zhang, Rev. Mod. Phys. **83**, 1057 (2011).

[2] X.-L. Qi, T. L. Hughes, and S.-C. Zhang, Phys. Rev. B **78**, 195424 (2008).

[3] F. D. M. Haldane, Phys. Rev. Lett. **61**, 2015 (1988).

[4] X. Wan, A. M. Turner, A. Vishwanath, and S. Y. Savrasov, Phys. Rev. B **83**, 205101 (2011).

[5] C. Chen, H. Wang, Z. Yang, and H. Zhang, Chin. Phys. Lett. **38**, 057302 (2021).

[6] L. Wu, M. Salehi, N. Koirala, J. Moon, S. Oh, and N. P. Armitage, Science **354**, 1124 (2016).

[7] D. Xiao, J. Jiang, J.-H. Shin, W. Wang, F. Wang, Y.-F. Zhao, C. Liu, W. Wu, M. H. W. Chan, N. Samarth, and C.-Z. Chang, Phys. Rev. Lett. **120**, 056801 (2018).

[8] D. Zhang, M. Shi, T. Zhu, D. Xing, H. Zhang, and J. Wang, Phys. Rev. Lett. **122**, 206401 (2019).

[9] C. Liu, Y. Wang, H. Li, Y. Wu, Y. Li, J. Li, K. He, Y. Xu, J. Zhang, and Y. Wang, Nat. Mater. **19**, 522 (2020).

[10] R. Li, J. Wang, X. L. Qi, and S. C. Zhang, Nat. Phys. **6**, 284 (2010).

[11] D. J. E. Marsh, K. C. Fong, E. W. Lentz, L. Šmejkal, and M. N. Ali, Phys. Rev. Lett. **123**, 121601 (2019).

[12] A. Sekine and K. Nomura, Phys. Rev. Lett. **116**, 096401 (2016).

[13] H. Sumiyoshi and S. Fujimoto, Phys. Rev. Lett. **116**, 166601 (2016).

[14] H. Ooguri and M. Oshikawa, Phys. Rev. Lett. **108**, 161803 (2012).

[15] K. Taguchi, T. Imaeda, T. Hajiri, T. Shiraishi, Y. Tanaka, N. Kitajima, and T. Naka, Phys. Rev. B **97**, 214409 (2018).

[16] T. Imaeda, Y. Kawaguchi, Y. Tanaka, and M. Sato, J. Phys. Soc. Jpn. **88**, 024402 (2019).

[17] J. Gooth, B. Bradlyn, S. Honnali, C. Schindler, N. Kumar, J. Noky, Y. Qi, C. Shekhar, Y. Sun, Z. Wang, B. A. Bernevig, and C. Felser, Nature (London) **575**, 315 (2019).

[18] D. M. Nenno, C. A. C. Garcia, J. Gooth, C. Felser, and P. Narang, Nat. Rev. Phys. **2**, 682 (2020).

[19] A. Sekine and K. Nomura, J. Appl. Phys. **129**, 141101 (2021).

[20] H. Li, H. Jiang, C.-Z. Chen, and X. C. Xie, Phys. Rev. Lett. **126**, 156601 (2021).

[21] Y. Xiao, H. Wang, D. Wang, R. Lu, X. Yan, H. Guo, C.-M. Hu, K. Xia, H. Zhang, and D. Xing, Phys. Rev. B **104**, 115147 (2021).

[22] T. Zhu, H. Wang, D. Xing, and H. Zhang, Phys. Rev. B **106**, 075103 (2022).

[23] J. Zhang, D. Wang, M. Shi, T. Zhu, H. Zhang, and J. Wang, Chin. Phys. Lett. **37**, 077304 (2020).

[24] H. Wang, D. Wang, Z. Yang, M. Shi, J. Ruan, D. Xing, J. Wang, and H. Zhang, Phys. Rev. B **101**, 081109(R) (2020).

[25] T. Zhu, H. Wang, H. Zhang, and D. Xing, npj Comput. Mater. **7**, 121 (2021).

[26] Y. Gong, J. Guo, J. Li, K. Zhu, M. Liao, X. Liu, Q. Zhang, L. Gu, L. Tang, X. Feng, D. Zhang, W. Li, C. Song, L. Wang, P. Yu, X. Chen, Y. Wang, H. Yao, W. Duan, Y. Xu *et al.*, Chin. Phys. Lett. **36**, 076801 (2019).

[27] M. M. Otrokov, I. I. Klimovskikh, H. Bentmann, D. Estyunin, A. Zeugner, Z. S. Aliev, S. Gass, A. U. B. Wolter, A. V. Koroleva, A. M. Shikin, M. Blanco-Rey, M. Hoffmann, I. P. Rusinov, A. Yu. Vyazovskaya, S. V. Eremeev, Yu. M. Koroteev, V. M. Kuznetsov, F. Freyse, J. Sánchez-Barriga *et al.*, Nature (London) **576**, 416 (2019).

[28] Y. Deng, Y. Yu, M. Z. Shi, Z. Guo, Z. Xu, J. Wang, X. H. Chen, and Y. Zhang, Science **367**, 895 (2020).

[29] B. Chen, F. Fei, D. Zhang, B. Zhang, W. Liu, S. Zhang, P. Wang, B. Wei, Y. Zhang, Z. Zuo, J. Guo, Q. Liu, Z. Wang, X. Wu, J. Zong, X. Xie, W. Chen, Z. Sun, S. Wang, Y. Zhang *et al.*, Nat. Commun. **10**, 4469 (2019).

[30] I. I. Klimovskikh, M. M. Otrokov, D. Estyunin, S. V. Eremeev, S. O. Filnov, A. Koroleva, E. Shevchenko, V. Voroshnin, A. G. Rybkin, I. P. Rusinov, M. Blanco-Rey, M. Hoffmann, Z. S. Aliev, M. B. Babanly, I. R. Amiraslanov, N. A. Abdullayev, V. N. Zverev, A. Kimura *et al.*, npj Quantum Mater. **5**, 54 (2020).

[31] J. Wang, R. Li, S.-C. Zhang, and X.-L. Qi, Phys. Rev. Lett. **106**, 126403 (2011).

[32] E. S. Dayhoff, Phys. Rev. **107**, 84 (1957).

[33] F. M. Johnson and A. H. Nethercot, Phys. Rev. **114**, 705 (1959).

[34] Y. R. Shen and N. Bloembergen, Phys. Rev. **143**, 372 (1966).

[35] P. A. Fleury and R. Loudon, Phys. Rev. **166**, 514 (1968).

[36] C. Kittel, Phys. Rev. **82**, 565 (1951).

[37] F. Keffer and C. Kittel, Phys. Rev. **85**, 329 (1952).

[38] Z.-L. Xiang, S. Ashhab, J. Q. You, and F. Nori, Rev. Mod. Phys. **85**, 623 (2013).

[39] M. Aspelmeyer, T. J. Kippenberg, and F. Marquardt, Rev. Mod. Phys. **86**, 1391 (2014).

[40] M. Scully and M. Zubairy, *Quantum Optics* (Cambridge, New York, 1997).

[41] M. O. Scully, Phys. Rev. Lett. **55**, 2802 (1985).

[42] C. Dong, V. Fiore, M. C. Kuzyk, and H. Wang, Science **338**, 1609 (2012).

[43] X. Zhang, C.-L. Zou, N. Zhu, F. Marquardt, L. Jiang, and H. X. Tang, Nat. Commun. **6**, 8914 (2015).

[44] F. R. Morgenthaler, Phys. Rev. Lett. **11**, 69 (1963).

[45] F. B. Anderson and H. B. Callen, Phys. Rev. **136**, A1068 (1964).

[46] Y. S. Gui, N. Mecking, and C. M. Hu, Phys. Rev. Lett. **98**, 217603 (2007).

[47] Y. Cao, P. Yan, H. Huebl, S. T. B. Goennenwein, and G. E. W. Bauer, Phys. Rev. B **91**, 094423 (2015).

[48] H. H. Jiang, Y. Xiao, C. M. Hu, H. Guo, and K. Xia, Nanotechnology **29**, 254002 (2018).

[49] H. Maier-Flaig, M. Harder, R. Gross, H. Huebl, and S. T. B. Goennenwein, Phys. Rev. B **94**, 054433 (2016).

[50] R. Serway and J. Jewett, *Physics for Scientists and Engineers* (Thomson, New York, 2008).

[51] H. Huebl, C. W. Zollitsch, J. Lotze, F. Hocke, M. Greifenstein, A. Marx, R. Gross, and S. T. B. Goennenwein, Phys. Rev. Lett. **111**, 127003 (2013).

[52] Y. Tabuchi, S. Ishino, T. Ishikawa, R. Yamazaki, K. Usami, and Y. Nakamura, Phys. Rev. Lett. **113**, 083603 (2014).

[53] M. Goryachev, W. G. Farr, D. L. Creedon, Y. Fan, M. Kostylev, and M. E. Tobar, Phys. Rev. Appl. **2**, 054002 (2014).

[54] X. Zhang, C.-L. Zou, L. Jiang, and H. X. Tang, Phys. Rev. Lett. **113**, 156401 (2014).

[55] L. Bai, M. Harder, Y. P. Chen, X. Fan, J. Q. Xiao, and C.-M. Hu, Phys. Rev. Lett. **114**, 227201 (2015).

[56] Y.-P. Wang, G.-Q. Zhang, D. Zhang, T.-F. Li, C.-M. Hu, and J. Q. You, Phys. Rev. Lett. **120**, 057202 (2018).

[57] J. Chen, C. Liu, T. Liu, Y. Xiao, K. Xia, G. E. W. Bauer, M. Wu, and H. Yu, Phys. Rev. Lett. **120**, 217202 (2018).

[58] S. Klingler, V. Amin, S. Geprägs, K. Ganzhorn, H. Maier-Flaig, M. Althammer, H. Huebl, R. Gross, R. D. McMichael, M. D. Stiles, S. T. B. Goennenwein, and M. Weiler, Phys. Rev. Lett. **120**, 127201 (2018).

[59] H. Qin, S. J. Hämäläinen, and S. van Dijken, Sci. Rep. **8**, 5755 (2018).

[60] Y.-P. Wang, J. Rao, Y. Yang, P.-C. Xu, Y. Gui, B. Yao, J. You, and C.-M. Hu, Phys. Rev. Lett. **123**, 127202 (2019).

[61] G. Scalari, C. Maissen, D. Turčinková, D. Hagenmüller, S. De Liberato, C. Ciuti, C. Reichl, D. Schuh, W. Wegscheider, M. Beck, and J. Faist, Science **335**, 1323 (2012).

[62] J. Li, Y. Li, S. Du, Z. Wang, B.-L. Gu, S.-C. Zhang, K. He, W. Duan, and Y. Xu, Sci. Adv. **5**, eaaw5685 (2019).

[63] Y.-J. Hao, P. Liu, Y. Feng, X.-M. Ma, E. F. Schwier, M. Arita, S. Kumar, C. Hu, R. Lu, M. Zeng, Y. Wang, Z. Hao, H.-Y. Sun, K. Zhang, J. Mei, N. Ni, L. Wu, K. Shimada, C. Chen, Q. Liu *et al.*, Phys. Rev. X **9**, 041038 (2019).

[64] Y. J. Chen, L. X. Xu, J. H. Li, Y. W. Li, H. Y. Wang, C. F. Zhang, H. Li, Y. Wu, A. J. Liang, C. Chen, S. W. Jung, C. Cacho, Y. H. Mao, S. Liu, M. X. Wang, Y. F. Guo, Y. Xu, Z. K. Liu, L. X. Yang, and Y. L. Chen, Phys. Rev. X **9**, 041040 (2019).

[65] H. Li, S.-Y. Gao, S.-F. Duan, Y.-F. Xu, K.-J. Zhu, S.-J. Tian, J.-C. Gao, W.-H. Fan, Z.-C. Rao, J.-R. Huang, J.-J. Li, D.-Y. Yan, Z.-T. Liu, W.-L. Liu, Y.-B. Huang, Y.-L. Li, Y. Liu, G.-B. Zhang, P. Zhang, T. Kondo *et al.*, Phys. Rev. X **9**, 041039 (2019).

[66] E. D. L. Rienks, S. Wimmer, J. Sanchez-Barriga, O. Caha, P. S. Mandal, J. Ruzicka, A. Ney, H. Steiner, V. V. Volobuev, H. Groiss, M. Albu, G. Kothleitner, J. Michalička, S. A. Khan, J. Minár, H. Ebert, G. Bauer, F. Freyse, A. Varykhalov, O. Rader *et al.*, Nature (London) **576**, 423 (2019).

[67] J. Wu, F. Liu, M. Sasase, K. Ienaga, Y. Obata, R. Yukawa, K. Horiba, H. Kumigashira, S. Okuma, T. Inoshita, and H. Hosono, Sci. Adv. **5**, eaax9989 (2019).

[68] R. C. Vidal, A. Zeugner, J. I. Facio, R. Ray, M. H. Haghighi, A. U. B. Wolter, L. T. Corredor Bohorquez, F. Caglieris, S. Moser, T. Figgemeier, T. R. F. Peixoto, H. B. Vasili, M. Valvidares, S. Jung, C. Cacho, A. Alfonsov, K. Mehlawat, V. Kataev, C. Hess, M. Richter *et al.*, Phys. Rev. X **9**, 041065 (2019).

[69] C. Hu, K. N. Gordon, P. Liu, J. Liu, X. Zhou, P. Hao, D. Narayan, E. Emmanouilidou, H. Sun, Y. Liu, H. Brawer, A. P. Ramirez, L. Ding, H. Cao, Q. Liu, D. Dessau, and N. Ni, Nat. Commun. **11**, 97 (2020).

[70] K. He, npj Quantum Mater. **5**, 90 (2020).

[71] G. Zhan, M. Shi, Z. Yang, and H. Zhang, Chin. Phys. Lett. **38**, 077105 (2021).